The Company of Biologists

RESEARCH ARTICLE

Super-resolution imaging of live sperm reveals dynamic changes of the actin cytoskeleton during acrosomal exocytosis

Ana Romarowski[1], Ángel G. Velasco Félix[2], Paulina Torres Rodríguez[3], María G. Gervasi[4], Xinran Xu[5], Guillermina M. Luque[1], Gastón Contreras-Jiménez[3], Claudia Sánchez-Cárdenas[3], Héctor V. Ramírez-Gómez[3], Diego Krapf[5], Pablo E. Visconti[4], Dario Krapf[6], Adán Guerrero[2], Alberto Darszon[3] and Mariano G. Buffone[1],*

ABSTRACT

Filamentous actin (F-actin) is a key factor in exocytosis in many cell types. In mammalian sperm, acrosomal exocytosis (denoted the acrosome reaction or AR), a special type of controlled secretion, is regulated by multiple signaling pathways and the actin cytoskeleton. However, the dynamic changes of the actin cytoskeleton in live sperm are largely not understood. Here, we used the powerful properties of SiR-actin to examine actin dynamics in live mouse sperm at the onset of the AR. By using a combination of super-resolution microscopy techniques to image sperm loaded with SiR-actin or sperm from transgenic mice containing Lifeact-EGFP, six regions containing F-actin within the sperm head were revealed. The proportion of sperm possessing these structures changed upon capacitation. By performing live-cell imaging experiments, we report that dynamic changes of F-actin during the AR occur in specific regions of the sperm head. While certain F-actin regions undergo depolymerization prior to the initiation of the AR, others remain unaltered or are lost after exocytosis occurs. Our work emphasizes the utility of live-cell nanoscopy, which will undoubtedly impact the search for mechanisms that underlie basic sperm functions.

This article has an associated First Person interview with the first author of the paper.

KEY WORDS: Acrosomal exocytosis, Actin, Sperm

INTRODUCTION

Exocytosis is the pathway by which cells selectively externalize compounds and, as such, it is essential for a number of basic biological processes. In spermatozoa, acrosomal exocytosis (also known as acrosome reaction, denoted AR), a special type of controlled secretion, is essential for fertilization in mammals (Dan, 1952). Sperm acquire the ability to undergo the AR in the female reproductive tract in a complex cascade of events all grouped under the name of capacitation (Puga Molina et al., 2018; Stival et al.,

[1]Instituto de Biología y Medicina Experimental (IBYME), Consejo Nacional de Investigaciones Científicas y Técnicas (CONICET), Buenos Aires C1428ADN, Argentina. [2]Laboratorio Nacional de Microscopía Avanzada, Instituto de Biotecnología, Universidad Nacional Autónoma de México (UNAM), Cuernavaca, Morelos 62210, México. [3]Departamento de Genética del Desarrollo y Fisiología Molecular, Instituto de Biotecnología, Universidad Nacional Autónoma de México (UNAM), Cuernavaca, Morelos 62210, México. [4]Department of Veterinary and Animal Science, Paige Labs, University of Massachusetts, Amherst, MA 01003, USA. [5]Department of Electrical and Computer Engineering, School of Biomedical Engineering, 1301 Campus Delivery, Fort Collins, CO 80523, USA. [6]Instituto de Biología Molecular y Celular de Rosario (CONICET-UNR), Rosario, Santa Fe S2000EZP, Argentina.

*Author for correspondence (mgbuffone@ibyme.conicet.gov.ar)

D.K., 0000-0002-2833-5553; M.G.B., 0000-0002-7163-6482

2015). The sperm AR occurs in mice in the upper segments of the female oviductal isthmus (Hino et al., 2016; La Spina et al., 2016; Muro et al., 2016) and is essential for the appropriate relocalization of proteins involved in sperm–egg fusion (Satouh et al., 2012).

Acrosomal exocytosis is a highly controlled event that consists of multiple stages that culminate in the membrane around the secretory vesicle being incorporated into the plasma membrane. At the molecular level, this complex exocytic process is regulated by several signaling pathways involving: (1) membrane potential (De La Vega-Beltran et al., 2012), (2) proteins from the fusion machinery system (Belmonte et al., 2016; De Blas et al., 2005), (3) small GTPases (Branham et al., 2009; Romarowski et al., 2015), (4) changes in ion concentration, where Ca^{2+} is a key player (Fukami et al., 2003; Romarowski et al., 2016a; Sánchez-Cárdenas et al., 2014), and (5) changes in the actin cytoskeleton (Brener et al., 2003; Romarowski et al., 2016b). In this regard, the expression of actin and several actin-related proteins in mammalian sperm (some of which are testis specific) suggests that actin polymerization and depolymerization are important for sperm function (Gervasi et al., 2018; Romarowski et al., 2016b).

Filamentous actin (F-actin) is a key factor in exocytosis in many cell types. It has been shown that F-actin holds together the molecular players of the secretory pathway, determines the precise site for granule exocytosis and shapes the exocytotic responses in secretory cells. In addition, stabilization of the actin network inhibits exocytosis, whereas depolymerization of this network increases the number of docked secretory granules and enhances the exocytotic response (Chowdhury et al., 1999; Ehre et al., 2004; Gasman et al., 2004; Muallem et al., 1995). As in somatic cells, the actin cytoskeleton of mammalian sperm is dynamic. While during sperm capacitation polymerization is predominant (Brener et al., 2003; Romarowski et al., 2015), during the AR, actin depolymerization occurs (Spungin et al., 1995).

Previous studies regarding actin polymerization/depolymerization were exclusively performed in fixed capacitated sperm or by means of using isolated membranes that had either been exposed or not to AR inducers (Brener et al., 2003; Romarowski et al., 2015). In addition, most studies evaluating F-actin in mammalian sperm were performed using phalloidin, which is toxic and not capable of crossing the cell plasma membrane of live cells (Cooper, 1987; Vandekerckhove et al., 1985; Visegrády et al., 2004). Thus, the phalloidin staining approach is not suitable to study this dynamic process in real time using live cells. However, recent reports have demonstrated the use of a novel membrane permeable fluorescent probe, called SiR-actin, that binds to actin filaments *in vivo* (Lukinavičius et al., 2014; Magliocca et al., 2017; Yamazaki et al., 2018). This probe allows one to image actin filaments without the need to overexpress fluorescently tagged proteins, such as Lifeact, actin monomers or actin-binding proteins. In addition, SiR-actin provides a high signal-to-noise ratio, facilitating the visualization of the finest details of the cortical actin network and it has been successfully

visualized in neurons in stimulated emission depletion (STED) super-resolution microscopy studies (D'Este et al., 2015).

By using this powerful new probe, we aimed to examine actin dynamics in live mouse sperm, specifically during the AR process. We hypothesize that a complex and highly regulated process, such as the AR, will be accompanied by specific changes in actin dynamics. To this end, in live-cell imaging experiments, we set up the conditions to simultaneously monitor actin cytoskeleton remodeling and AR occurrence by monitoring SiR-actin and FM4-64, respectively (Mata-Martínez et al., 2018; Romarowski et al., 2016a; Sánchez-Cárdenas et al., 2014). For the first time, we report the observation of acrosomal exocytosis via super-resolution microscopy in real time. Our work provides a detailed characterization of the F-actin cytoskeleton in the sperm head by using SiR-actin in combination with different super-resolution microscopy approaches and transgenic mice containing the F-actin-binding protein Lifeact-EGFP. Additionally, we observed dynamic changes of F-actin in restricted regions of the sperm head prior to and after the initiation of the AR. Finally, our work emphasizes the advantage of live-cell nanoscopy for the study of ultra-structures in sperm as well as in other cell types. These imaging capabilities will undoubtedly impact the study of mechanisms that underlie basic sperm functions.

RESULTS
SiR-actin, a new versatile tool to visualize F-actin in mouse sperm
To study the organization of F-actin in mouse sperm, we exploited the membrane permeability of SiR-actin. Because SiR-actin is produced as a modified form of jasplakinolide, a drug that is normally used to stabilize polymerized actin *in vitro*, it is recommended to minimize the concentration of the probe and ideally not have a concentration of >100 nM, since higher concentrations could affect the actin cytoskeleton dynamics (Lukinavičius et al., 2014). For this reason, we incubated sperm with increasing concentrations of SiR-actin (50 to 500 nM). Although 500 nM of SiR-actin resulted in a bright fluorescent signal in the sperm head and flagellum, we found that 100 nM SiR-actin (in accordance with the manufacturer's recommendations to avoid artifacts) showed a good signal-to-noise ratio (Fig. 1A). The signal observed using 50 nM was barely detectable. As a control, cells that were not loaded with SiR-actin displayed no fluorescence (auto-fluorescence was not significant when excited by the far-red wavelength used to detect SiR-actin; data not shown). Analysis of sperm motility by computer-assisted sperm analysis (CASA) was used to evaluate whether 100 nM of SiR-actin affected sperm motility and viability. As shown in Fig. S1, this probe concentration did not alter either the viability or sperm motility.

F-actin is normally visualized in fixed mammalian sperm by using fluorophore-conjugated phalloidin. To compare the staining produced by phalloidin and SiR-actin, we loaded the cells with both probes. By using confocal microscopy, we found that unlike phalloidin, which stains the sperm head homogenously, SiR-actin shows F-actin structures in specific regions of the sperm head (Fig. 1B).

Previous studies from several laboratories report an increase in actin polymerization during capacitation in both the head and the
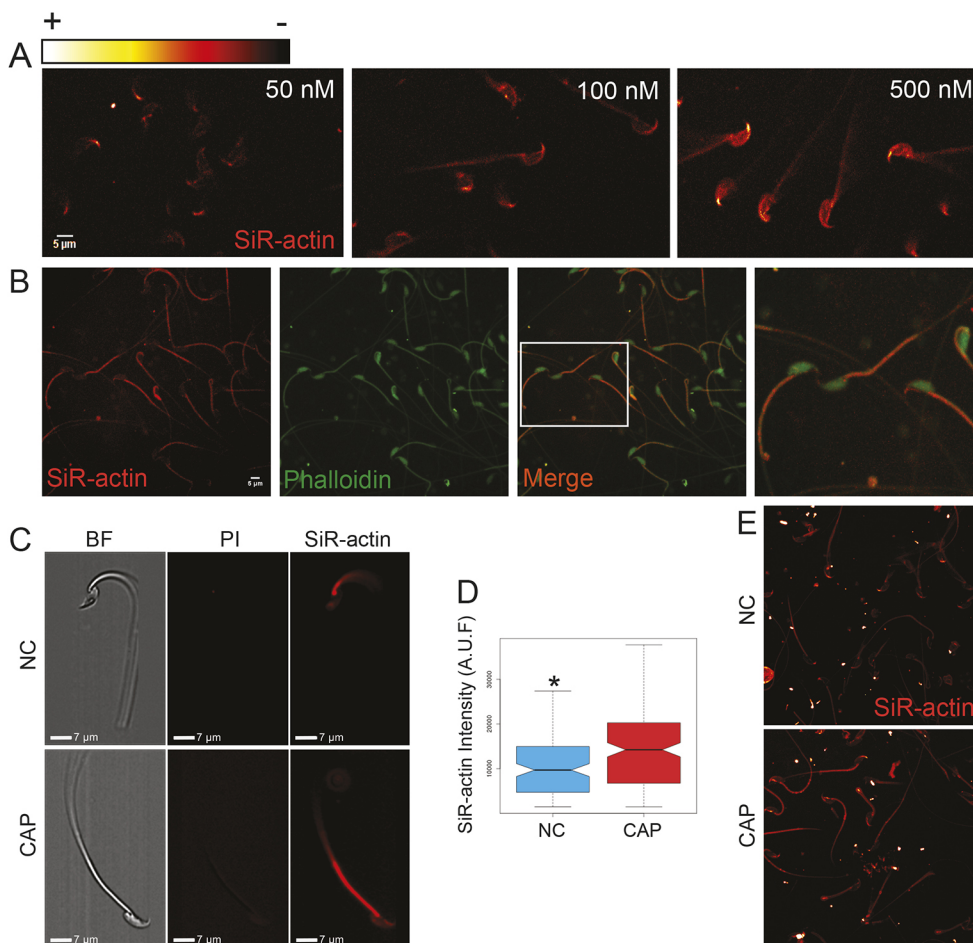

Fig. 1. SiR-actin, a novel method to visualize F-actin in mature mouse sperm. (A) Representative images of sperm loaded with different SiR-actin concentrations (50–500 nM). Fluorescence intensities are represented as a color map, see reference bar on top of panel A; weak (–) to strong (+) fluorescence. (B) Representative images of sperm labeled with both SiR-actin and Alexa-Fluor-488–phalloidin. The image on the right is a magnification of the boxed area in the merged picture. n=3. (C) Representative images obtained by image-based flow cytometry for non-capacitated (NC) and capacitated (CAP) sperm showing the bright field (BF), the PI and the SiR-actin channels. (D) Box plot of a representative experiment comparing NC and CAP sperm. The box represents the 25–75th percentiles, and the median is indicated. The whiskers show 1.5 times the interquartile range; the notches represent the 95% confidence interval around the median. Statistical analysis was performed using a Kolmogórov-Smirnov test. *P<0.05. AUF, arbitrary units of fluorescence. A summary of all experiments can be seen in Fig. S2E, n=12 mice. (E) Representative images of SiR-actin loaded sperm before and after 60 min incubation under CAP and NC conditions (n=3).

tail of mouse sperm. To further investigate whether SiR-actin can also reveal F-actin formation during sperm capacitation, cells were loaded with SiR-actin and incubated under capacitating and non-capacitating conditions, and analyzed via image-based flow cytometry. The settings used to perform these experiments are shown in Fig. S2. This analysis confirmed previous observations obtained using phalloidin. The fluorescence intensity of sperm incubated under capacitating conditions was significantly higher than in the non-capacitated cells, indicating actin polymerization during this process (Fig. 1C,D; Fig. S2E). Similar results were obtained using confocal microscopy (Fig. 1E).

SiR-actin reveals novel F-actin structures in the sperm head
Using confocal microscopy, we found six different F-actin structures within the sperm head as follows: (1) the perforatorium, staining in the more apical tip of the head; (2) the lower acrosome, labeling in the acrosomal region close to the anterior tip of the head; (3) the upper acrosome, staining over the entire cortical acrosomal cap; (4) a ventral, fluorescent signal in the lower edge of the head; (5) the septum, a clear fluorescent boundary between the equatorial and post-acrosomal segment; (6) a neck, a focused signal in the neck region. These patterns are represented in the schematic diagram shown in Fig. 2A.

When we compared the percentage of sperm that displayed each of these patterns under capacitating vs non-capacitating conditions, no significant differences were observed (Fig. 2B). To further characterize the distribution of these patterns in the whole population, we analyzed whether they were correlated in non-capacitated and capacitated sperm, using a correlation matrix of the six patterns defined above (Fig. 2C). A positive correlation coefficient would thus imply the structures are more likely to be present together and a negative correlation would imply one structure is more likely to be present in the absence of the second one. In non-capacitated sperm, the pairs of patterns upper acrosome/septum, septum/neck and neck/lower acrosome were significantly positively correlated. In contrast, the ventral region was negatively correlated with the neck. Strikingly, all these correlations disappeared upon sperm capacitation, revealing changes undertaken by the actin cytoskeleton. In capacitated sperm, no significantly positively correlated patterns were observed and the negatively correlated pairs were ventral/perforatorium and upper acrosome/lower acrosome.

As we observed great heterogeneity in the sperm population, with most of the cells displaying two or more patterns simultaneously, we classified the cells using a six-position binary code developed specifically for this purpose (Fig. 2A). The binary code was defined as 1 or 0 (presence or absence of signal at a given region, respectively). In addition, each position in the 6-digit code represents one of the patterns. Using this code, we evaluated the proportion of each combination of patterns in non-capacitated and capacitated sperm and found that five of them were significantly different between these two conditions (Fig. 2D). In the chart of Fig. 2E, the five pattern combinations that increase or decrease during capacitation can be observed. Those five patterns are shown in the representative pictures of Fig. 2F. The arrows indicate the increase or decrease of these patterns during capacitation (pointing upward or downward, respectively) (Fig. 2F).

Similar F-actin structures are observed in transgenic Lifeact-EGFP mice
Because SiR-actin revealed novel F-actin structures in the sperm head that are not observed when staining via the widely used phalloidin, we aimed to visualize these structures in sperm from transgenic Lifeact-EGFP mice (Riedl et al., 2010). Lifeact is a 17-amino-acid peptide, which stains F-actin structures in eukaryotic cells and tissues, which does not interfere with actin dynamics *in vitro* and *in vivo*.

Lifeact-EGFP sperm displayed a strong fluorescent signal in the head and in the tail. The fluorescent signal in the flagellum is mostly from the mid-piece, but F-actin is also visible in the principal piece. Using sperm from Lifeact-EGFP transgenic mice, we observed F-actin structures in the sperm head with a similar localization to that seen in SiR-actin loaded sperm (Fig. 3A). These results suggest that the novel F-actin structures revealed by SiR-actin are not artifacts.

F-actin localization in the sperm head using STORM super-resolution microscopy
To investigate and further corroborate the organization of F-actin in the sperm head in more detail, we used the super-resolution imaging technique stochastic optical reconstruction microscopy (STORM), which has previously been used to visualize flagellar proteins in mouse sperm, such as CatSper proteins (Chung et al., 2014, 2017; Gervasi et al., 2018). We utilized this approach to study the distribution of F-actin in the sperm head. Because it is not possible to use STORM with SiR-actin, owing to its optical properties, we used phalloidin–Alexa-Fluor-647-stained sperm and recorded a very similar F-actin distribution to that observed with the SiR-actin probe (Fig. 3B). This result further validates the novel F-actin structures in the sperm head revealed by SiR-actin. Also, these experiments demonstrated the advantage of using super-resolution microscopy to reveal F-actin structures in the sperm head that otherwise displayed a homogeneous distribution due to the diffraction-limited acquisition of these images.

To visualize the three-dimensional F-actin distribution in the sperm head, the molecular localizations found by STORM in *xyz* coordinates were used to build *z* stacks of 2D *x-y* reconstructions, which were later rendered into a 3D image through the 3D viewer plugin in ImageJ. 3D-reconstructed videos can be observed in Movies 1 and 2.

Super-resolution microscopy of F-actin and plasma membrane using SiR-actin in combination with FM4-64
To obtain sub-diffraction images of the F-actin network using SiR-actin, we employed a recently developed variation of the localization technique, the Bayesian analysis of Blinking and Bleaching (3B), which allows analysis of data with multiple overlapping fluorophores in every image (Cox et al., 2012). Cells loaded with SiR-actin were also stained with the plasma membrane dye FM4-64 used for visualization of exocytosis and endocytosis (Romarowski et al., 2016a; Sánchez-Cárdenas et al., 2014). The images were obtained via TIRF microscopy (Fig. 4A,B) followed by 3B reconstruction (Fig. 4C). The areas delimited in Fig. 4C are shown in higher magnification in Fig. 4D–G. As shown in Fig. 4D and F, by applying this reconstruction algorithm, it is possible to observe in great detail the cortical actin structure (green) underneath the plasma membrane (magenta) in both the acrosomal area and the neck-midpiece region. In addition, the perforatorium region, which is localized at the very tip of the sperm head, possessed a well-defined F-actin structure whose function is unknown (Fig. 4E). Fig. 4G shows the F-actin structure localized at the boundary between the equatorial region and the post-acrosomal area (previously called 'septum') (see also Fig. 2A).
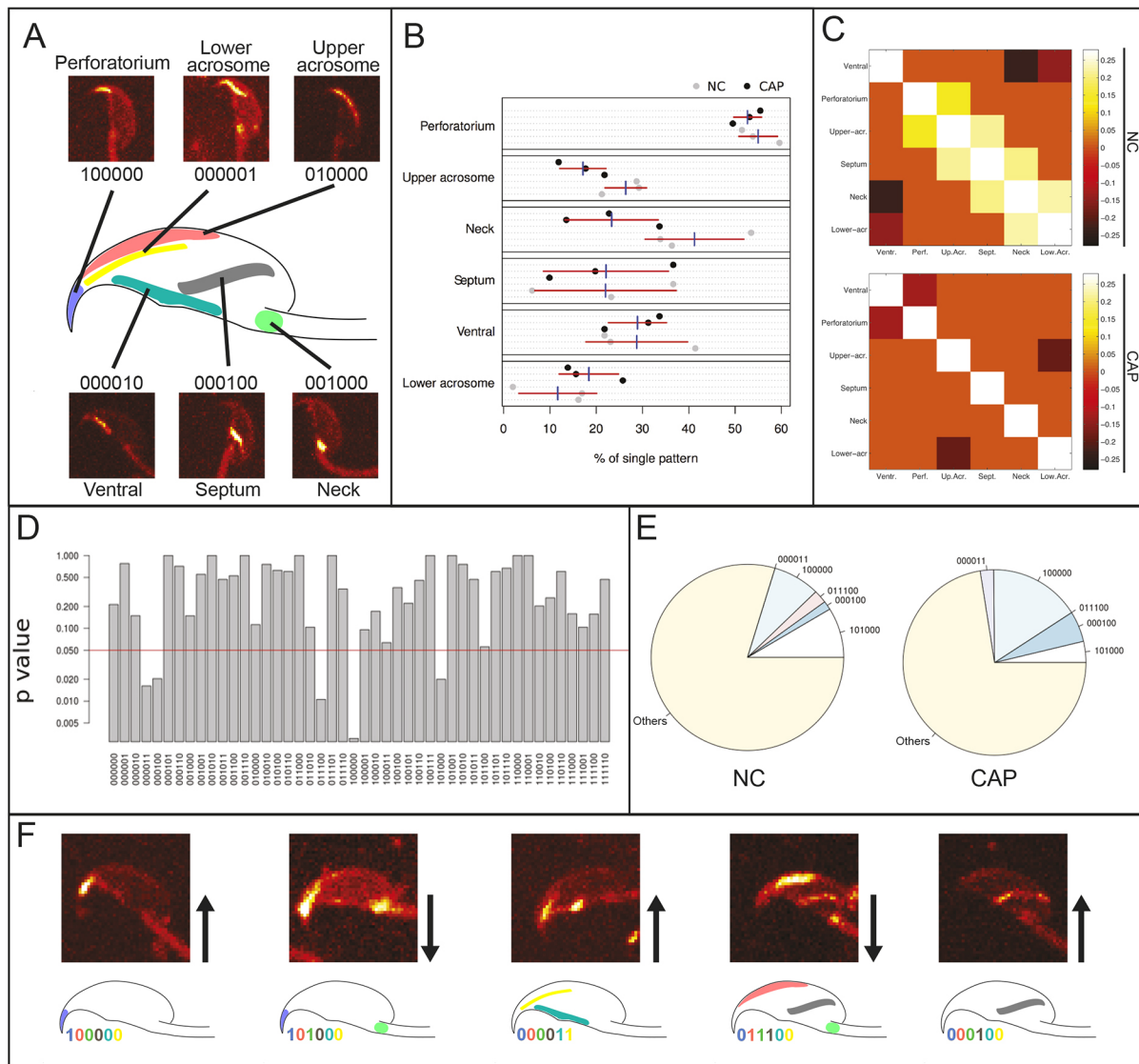
Fig. 2. SiR-actin reveals novel F-actin structures in the sperm head. (A) Representative diagram showing the six different F-actin structures within the sperm head that we denote as the perforatorium, lower acrosome, upper acrosome, ventral, septum and neck. A representative confocal image of each pattern is displayed. A binary code was used to determine the presence of these patterns in all the individual cells assessed. The binary code was defined as 1 (presence of signal at a given region) or 0 (absence of fluorescent signal). In addition, each position in the 6-digit code represents one of the patterns: the positions (from left to right) are assigned to perforatorium, upper acrosome, neck, septum, ventral and lower acrosome. (B) The proportion of each individual pattern in NC and CAP sperm was evaluated. Dots represent the mean from each mouse; the blue lines represent the median and the red lines are the s.d. from all the experiments conducted. Student's t-test was performed; $n=3$, analyzed cells=600. The P values originated in this statistical comparison were: 0.49 for perforatorium, 0.076 for upper acrosome, 0.1 for neck, 0.99 for septum, 0.99 for ventral and 0.34 for lower acrosome. (C) Correlation matrix of the six patterns in non-capacitated (NC) and capacitated (CAP) sperm. The hypothesis that the correlation coefficients (correlation matrix elements) were significantly different than zero was tested. To facilitate the observation of significant correlations, all the matrix elements without at least 5% correlation significance were set to zero. In NC sperm, the positively correlated pairs had P-values of <0.003, while the negative correlation had $P<0.0005$. In CAP sperm, the negative correlation of ventral/perforatorium and upper acrosome/lower acrosome had $P<0.02$ and $P=0.0006$, respectively. Student's t-test was performed; $n=3$, 221 non-capacitated sperm and 342 capacitated sperm were analyzed. (D) By using the binary code, the proportion of each pattern combination in NC and CAP sperm was evaluated. Only five pattern combinations are significantly different between these two conditions (those that are below the red line representing $P<0.05$). The P-values originated from this statistical comparison are represented in the y-axis of the graph. In the x-axis, each individual pattern combination is represented. Fisher's test was performed; $n=3$, analyzed cells=600. (E,F) Pie chart (E) showing the five pattern combinations that increase or decrease their proportion during capacitation. Those five pattern combinations are shown in the representative pictures (F). The arrows indicate the increase or decrease of these pattern combinations during capacitation (pointing upward or downward, respectively).

Highlighting the powerful capabilities of using super-resolution microscopy to study these processes, we observed changes in the F-actin network in or surrounding the perforatorium area. When we compared the super-resolution images of non-capacitated and capacitated sperm, we found that the perforatorium F-actin cytoskeleton undergoes structural modifications during capacitation

(Fig. S3). The well-defined F-actin structure observed prior to capacitation is altered, resulting in a more diffuse staining over that area. These type of observations cannot be visualized using conventional confocal microscopy alone, indicating that there is active actin remodeling in this structure during the capacitation process. Therefore, these results highlight the powerful capabilities
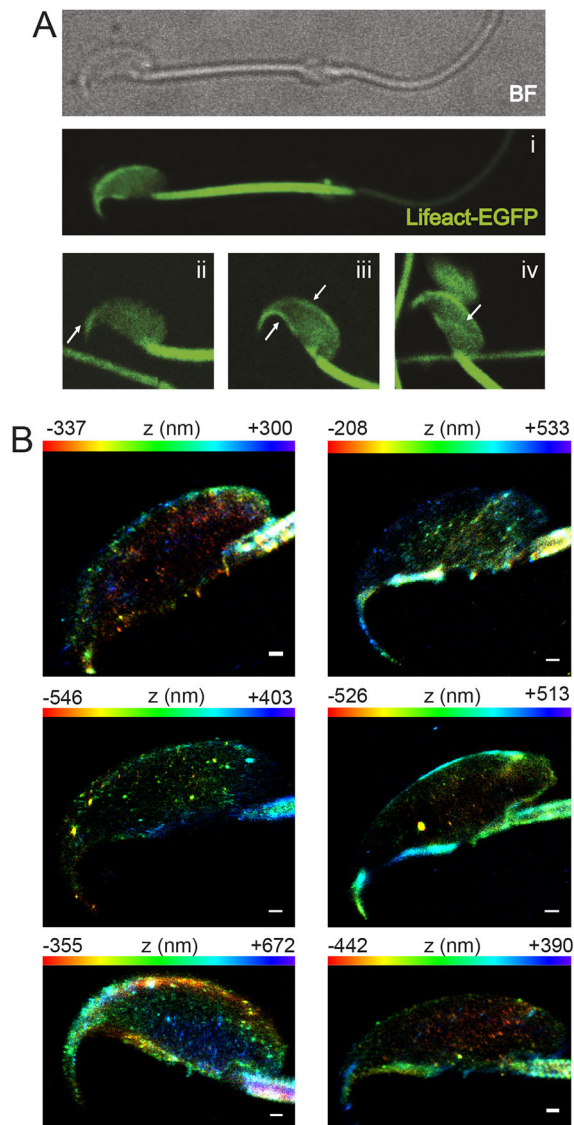
Fig. 3. F-actin visualization in the sperm head using Lifeact-EGFP transgenic sperm, and STORM super-resolution microscopy using phalloidin. (A) Non-capacitated sperm from Lifeact-EGFP mice displayed similar F-actin structures as observed with SiR-actin. Lifeact-EGFP sperm displayed a strong fluorescent signal in the head and in the tail (i). The fluorescent signal in the flagellum is mostly from the mid-piece, but F-actin is also visible in the principal piece. The arrows indicate different structures also observed when using SiR-actin, such as the perforatorium (ii), ventral and upper acrosome (iii) and septum (iv). BF, bright field. (n=3). (B) Representative images of 3D STORM super-resolution microscopy of F-actin in mouse sperm. Scale bar: 500 nm. Non-capacitated sperm were stained with Alexa-Fluor-647–phalloidin. Six representative images revealing the distribution of F-actin in the sperm head are shown (n=13). The 3D-reconstruction is colored according to the localization height as indicated in the color map. The 3D-reconstruction videos can be observed in Movies 1 and 2.

of super-resolution microscopy to visualize cytoskeletal structures in the mouse sperm head.

Dynamic changes of F-actin during acrosomal exocytosis occur in specific regions of the sperm head

In the following experiments, we aimed to visualize dynamic changes of the actin cytoskeleton during the AR, with emphasis on observing the depolymerization of the F-actin structure at the onset

of this event. Live sperm loaded with SiR-actin and FM4-64 were immobilized in concanavalin A-coated slides as previously described (Hirohashi et al., 2015; Romarowski et al., 2016a), to continuously monitor changes in SiR-actin in those cells that undergo exocytosis (as judged by the increase in the FM4-64 fluorescence). An agonist of the AR, such as the Ca^{2+} ionophore ionomycin, was added to trigger the initiation of the AR. Cells were recorded at 37°C for 20 min, as described in the corresponding Materials and Methods section. Following acquisition, the images were reconstructed using 3B analysis.

Our observations reveal that, among the six F-actin structures in the head that were described above, three of them change during AR: (1) the septum, (2) the lower acrosome and (3) the upper acrosome. Interestingly, the changes in these regions occurred with different kinetic behaviors as below.

Septum

Fig. 5A shows a representative super-resolution image of a sperm that, at the beginning of the recording, possesses the septum F-actin structure previously described (left). The time course sequence of that structure after the addition of ionomycin is shown at higher magnification. The regions of interest (ROIs) corresponding to the septum region (for SiR-actin) and the whole sperm head (for FM4-64) (Fig. 5B) are shown together with the corresponding fluorescence traces (Fig. 5C). The fluorescence curves indicate that F-actin depolymerization in the septum area preceded the AR initiation by ∼100 s (Fig. 5C). Fig. S4A–C illustrates a representative sequence of images of a sperm that did not initiate the AR and conserved the F-actin structure in that region. A video associated with this cell that loses the septum F-actin structure can be observed in the Movie 3.

Lower acrosome

This region also depolymerized before the initiation of the AR (see Fig. 5D). Fig. 5D displays a representative super-resolution sequence of images of a sperm that underwent actin depolymerization in this region after stimulation with ionomycin, prior to AR initiation. The ROIs corresponding to the lower segment region (for SiR-actin) and the whole sperm head (for FM4-64) are shown together with the corresponding fluorescence traces (Fig. 5E and F, respectively). These curves show that the depolymerization in the lower acrosome area also preceded the initiation of the AR by ∼50 s (Fig. 5F). A representative sequence of images of a sperm that did not initiate the AR and conserved the F-actin structure in the lower acrosomal region is shown in Fig. S4D–F. A video associated with this cell that loses the lower acrosome F-actin structure can be observed in Movie 4.

Upper acrosome

This region also displayed a loss of SiR-actin fluorescence intensity during the AR. As shown in Fig. 6B, the F-actin network that resembles the subcortical F-actin localization (also shown in Fig. 4D), is disassembled during the AR. However, analysis of the ROI corresponding to the upper acrosome area (Fig. 6A) and the resulting fluorescent traces (Fig. 6C) revealed that F-actin loss occurred ∼400 s after AR initiation, as judged by the increase in FM4-64 fluorescence. Similar to what was observed in the other two regions that displayed depolymerization during the AR, sperm that did not initiate the AR conserved the F-actin structure in the upper acrosomal region (Fig. S4G–I).

The decrease in SiR-actin fluorescence observed in the upper acrosome occurred several seconds after initiation of the AR,
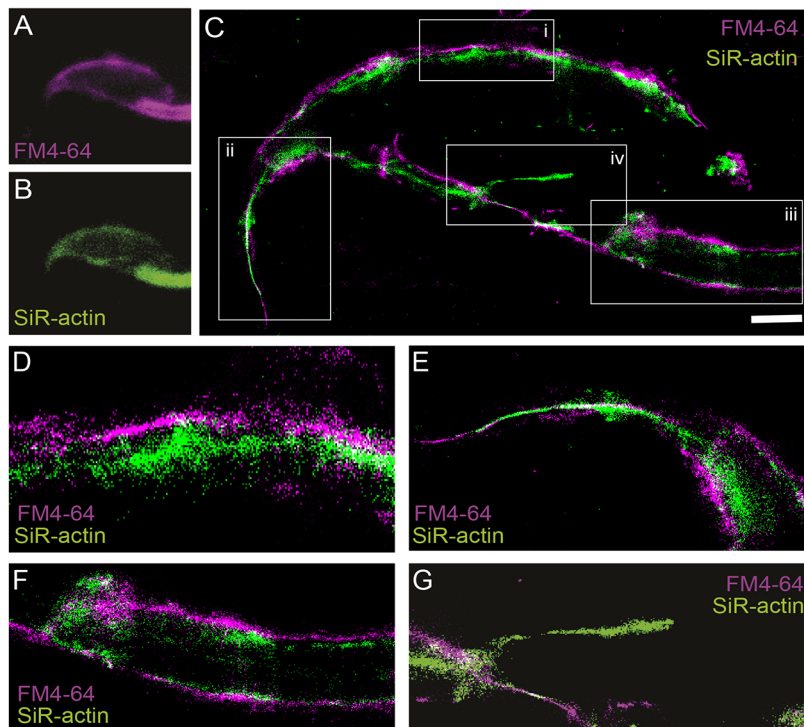
Fig. 4. Visualization of F-actin and plasma membrane in mouse sperm by super-resolution microscopy. (A,B) Diffraction-limited images obtained by TIRF microscopy of a sperm loaded with FM4-64 (A) and SiR-actin (B). (C) To obtain sub-diffraction resolution of F-actin using SiR-actin, we employed 3B analysis. The 3B super-resolution reconstruction of the sperm shown in A and B, after merging the two fluorescence channels. Scale bar: 1 µm. F-actin (revealed by SiR-actin) is shown in green and the plasma membrane (stained with FM4-64) in magenta. The areas depicted in C are shown in higher magnification in D–G. (D) Higher magnification of the area (i) showing the cortical F-actin network in close association with the plasma membrane. (E) Higher magnification of the area (ii) showing the F-actin localized in the perforatorium. (F) Higher magnification of the area (iii) showing F-actin present in the sperm neck. (G) Higher magnification of the area (iv) showing the septum F-actin structure.

suggesting that F-actin loss may occur as a result of membrane vesiculation, and that release of the protein is caused by the AR. Supporting this hypothesis, super-resolution analysis of sperm that initiated the AR revealed that cortical actin remained unaltered during the initial steps of membrane vesiculation. The time course of the formation of a hybrid vesicle during AR initiation is illustrated in Fig. 6D,E. A clear decrease in FM4-64 fluorescence and SiR-actin is observed as a result of membrane loss (see right arrow in panel 109.8 s). The membrane lost in that region is observed in the newly formed vesicle together with the F-actin that left the cortical actin in the sperm head (see left arrow in panel 109.8 s).

To further validate our results, we analyzed the fate of these three F-actin structures during the AR induced with another agonist, progesterone. Results obtained with progesterone were overall similar to those observed with Ca^{2+} ionophore; sperm undergoing the AR displayed loss of SiR-actin fluorescence in the septum, and lower and upper acrosome regions (Fig. S5). However, their kinetics were slightly different. The loss of F-actin in the septum and lower acrosome occurred ~400 s and ~40 s before the initiation of the AR, respectively. In the case of the upper acrosome, we observed that the loss of SiR-actin fluorescence occurred at about the same time of the FM4-64 fluorescence increase. The other regions containing F-actin (ventral, perforatorium and neck) did not change in sperm undergoing exocytosis (Fig. S6). The differences observed may be related to distinct mechanisms that these two agonists drive to stimulate the AR.

Specific F-actin structures in the sperm head did not change as a consequence of the AR

While three specific regions (septum, lower acrosome and upper acrosome) showed actin depolymerization or loss accompanying the AR, the other three F-actin structures in the head (ventral, perforatorium and neck) remained unchanged even though sperm underwent AR. Fig. 7 shows a representative sequence of images of sperm that were stimulated with ionomycin and that at the beginning

of the recording possessed the F-actin structure corresponding to the perforatorium (Fig. 7A–C), ventral or neck region (Fig. 7D–F). The ROIs corresponding to those regions (for SiR-actin) and the whole sperm head (for FM4-64) are shown (Fig. 7A, and D), together with the corresponding fluorescence traces (Fig. 7C and F). These traces show that depolymerization did not occur before or after the initiation of the AR.

DISCUSSION

Once capacitation takes place, mammalian sperm are ready for a regulated AR. Although the identity of the physiological AR inducer *in vivo* is controversial (Buffone et al., 2014), most authors agree on postulating Ca^{2+} elevation as one of the initial events leading to exocytosis. However, between the rise of intracellular Ca^{2+} and exocytosis, there is a lag period indicating that exocytosis in sperm relies on other signaling pathways downstream of the increase in Ca^{2+} (Romarowski et al., 2016a). Among them, we can highlight the involvement of phospholipases (Cohen et al., 2004; Fukami et al., 2001), cAMP (Branham et al., 2006; De Jonge et al., 1991; Lucchesi et al., 2016), exchange factors (i.e. EPAC) (Branham et al., 2009), Rab3A and SNARE proteins (De Blas et al., 2005; Quevedo et al., 2016), small GTPases (Baltiérrez-Hoyos et al., 2012; Belmonte et al., 2016; Fiedler et al., 2008; Pelletán et al., 2015; Romarowski et al., 2015) and depolymerization of the actin cytoskeleton formed during capacitation (Brener et al., 2003; Spungin et al., 1995). In this paper, we focused on observing specific dynamic changes of the F-actin network at the onset of the AR. Here, we showed actin depolymerization in specific regions of the sperm head during the AR, an event that was not observed before owing to technological limitations. Our approach used super-resolution microscopy in live cells where specific changes in F-actin are monitored in real time at the onset of the AR.

We used SiR-actin, a recently developed probe, to monitor F-actin dynamics in live cells (D'Este et al., 2015). The ability to use live sperm in our experiments as opposed to the use of traditional
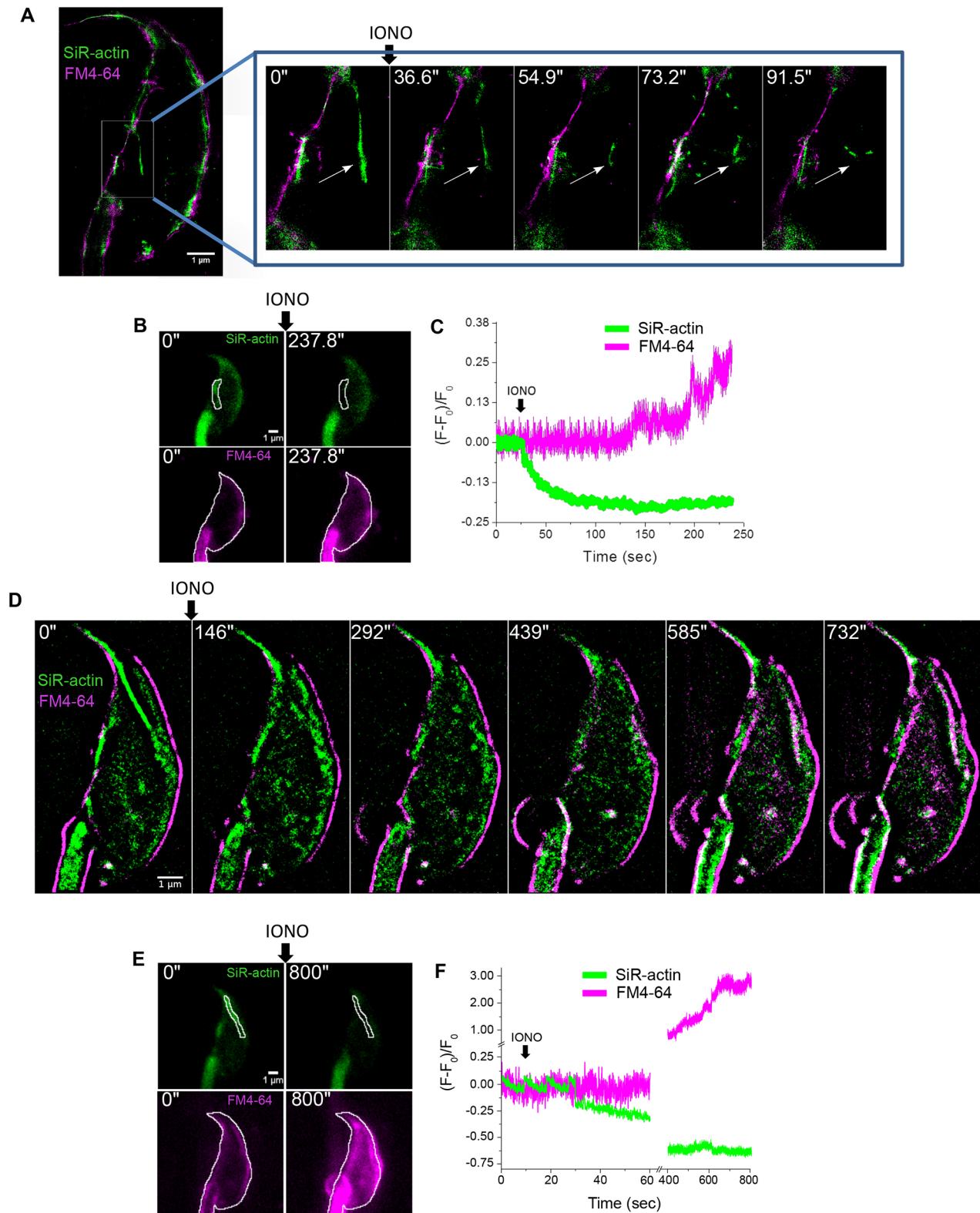
Fig. 5. See next page for legend.

phalloidin staining in fixed cells, revealed detailed spatio-temporal information about F-actin. These observations were consistent with similar results obtained in sperm from transgenic mice containing Lifeact-EGFP, and with data from super-resolution methods [STORM, super-resolution radiality fluctuations (SRRF) and 3B]

allowing detailed spatial localization of the actin network. We observed six different regions within the sperm head that are enriched in polymerized actin. One of them is the perforatorium, a prominent feature of falciform-shaped sperm heads, such as those found in mice. The perforatorium in mice has the shape of a curved

Fig. 5. Specific dynamic changes in the actin cytoskeleton before acrosomal exocytosis. Sperm were loaded with SiR-actin (green) and FM4-64 (magenta) and attached to concanavalin A-coated slides for imaging. Following acquisition, images were analyzed using 3B analysis. (A) Representative super-resolution image of a sperm that, at the beginning of the recording, possesses the septum F-actin structure previously described (left). In higher magnification, the time course sequence of that structure after addition of ionomycin (black arrow) is shown. The F-actin structure in the septum region depolymerizes prior to the initiation of the AR. ″ represents time in seconds. The white arrows highlight the F-actin structure in the septum region. (B,C) The ROIs corresponding to the septum region (for SiR-actin) and the whole sperm head (for FM4-64) (B) are shown together with the corresponding fluorescence traces (C). The corresponding movie for this experiment is shown in Movie 3. (D) Representative super-resolution images of a sperm that undergoes actin depolymerization in the lower acrosome region after stimulation with 10 μM of ionomycin prior to the initiation of the AR. (E,F) The ROIs corresponding to the lower acrosome region (for SiR-actin) and the whole sperm head (for FM4-64) (E) are shown together with the corresponding fluorescence traces (F). The corresponding movie for this experiment is shown in Movie 4 (n=6; 62 cells analyzed).

triangular rod at the apex of the sperm head, and splits into three interconnected prongs, one dorsal and two ventral, as it passes over the nucleus (Clermont et al., 1990). Although the function of sperm ultrastructural elements are poorly understood, it is thought that they play a mechanical role during egg penetration in fertilization (Korley et al., 1997). The presence of cytoskeletal structures in this sperm region, which is mostly occupied by the perinuclear theca, has been documented previously (Clermont et al., 1990). Besides these cytoskeletal structures, the components of this region are largely unknown (Korley et al., 1997; Oko and Morales, 1994). Protein FABP9 has been invoked as being a critical building block

for perinuclear theca organization and sperm plasma membrane attachment to those underlying structures (Selvaraj et al., 2009). Our studies revealed the presence of F-actin in this region that remains unaltered during the AR.

We also found that the proportion of sperm with a pattern that includes the perforatorium F-actin structure increased with capacitation (Fig. 2). Interestingly, super-resolution analysis of the F-actin network in this region showed subtle differences between non-capacitated and capacitated sperm (Fig. S3). The F-actin structure in capacitated sperm looked more diffuse compared to the well-defined structure in non-capacitated cells, suggesting that actin reorganization took place in that specific region during capacitation. Additional experiments will be necessary to understand the implication of this change in the mechanisms related to the AR and fertilization. However, because we previously observed that most sperm that undergo the AR initiate the Ca^{2+} increase in that region of the cell (Romarowski et al., 2016a), we speculate that changes in the actin network may modulate the Ca^{2+} wave associated with the AR. In this regard, the influence of the cytoskeleton in Ca^{2+} wave propagation and permeability has been previously reported in other systems (Torregrosa-Hetland et al., 2011).

In somatic cells, membrane-associated cytoskeletal components have been implicated in organizing membrane domains by providing lipid and protein tethers within the membrane (Suzuki et al., 2017). Another F-actin structure revealed by SiR-actin is localized at the boundary between the equatorial segment and the post-acrosomal region. Previous studies have demonstrated the presence of a physical barrier in that region that impeded normal lipid diffusion (Jones et al., 2007). This physical barrier in sperm is
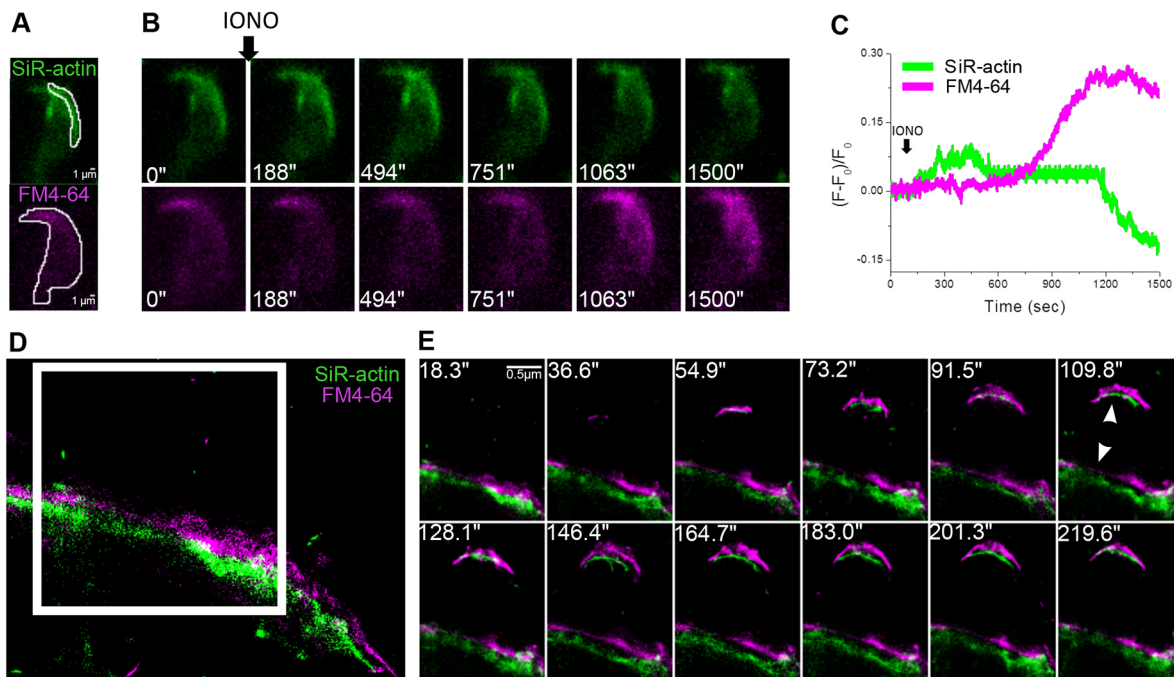

Fig. 6. Specific dynamic changes in the actin cytoskeleton after initiation of acrosomal exocytosis. (A) Sperm labeled with SiR-actin (green) and FM4-64 (magenta). The ROIs used for the analysis, corresponding to the upper acrosome region (for SiR-actin) and the whole sperm head (for FM4-64), are depicted. (B) Representative sequence of images of a sperm loaded with SiR-actin and FM4-64 that displayed a decrease in SiR-actin fluorescence in the upper acrosome region after stimulation with 10 μM ionomycin (addition indicated by black arrow). ″ represents time in seconds. (C) The resulting fluorescence traces revealed that the loss of F-actin occurred after the initiation of the AR as judged by the increase in FM4-64 fluorescence (n=6; 62 cells analyzed). (D,E) Super-resolution analysis of a sperm loaded with SiR-actin and FM4-64 showing the formation of a hybrid vesicle at the onset of the AR. The area depicted in D is shown at a higher magnification in E, at different times after 10 μM ionomycin addition. The cortical actin remained unaltered during the initial steps of membrane vesiculation. The arrows in the panel at 109.8 s indicate a clear decrease in FM4-64 fluorescence and SiR-actin as well as the newly formed vesicle containing both F-actin and plasma membrane. See Movie 5.
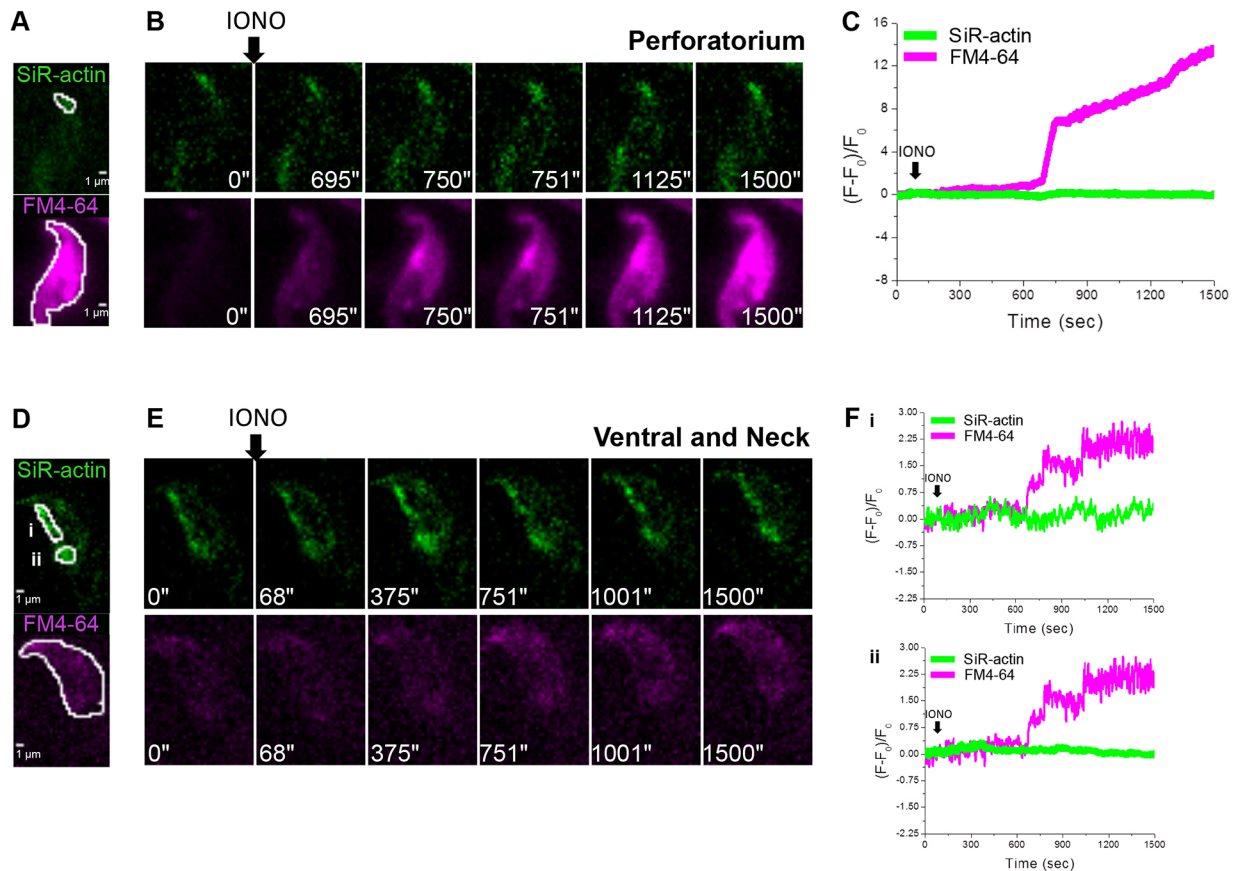
Fig. 7. Specific F-actin structures in the sperm head did not change as a consequence of the AR initiation. Sperm were loaded with SiR-actin (green) and FM4-64 (magenta) and attached to concanavalin A-coated slides for imaging using TIRF microscopy. Following image acquisition, the ROIs indicated in A and D were analyzed. Representative image sequences of sperm stimulated with ionomycin (addition indicated by black arrow) that initially possessed the F-actin structure corresponding to the perforatorium (B), ventral (D; i) or neck (D; ii) region. The corresponding fluorescence traces (C and F) of the indicated ROIs (for SiR-actin) and the whole sperm head (for FM4-64) (A and D) are shown on the right. Analysis of these traces demonstrates that the depolymerization did not occur before or after the initiation of the AR (C and F) (n=6. 62 cells analyzed).

composed of an electron-dense matrix, forming a demarcation line between both compartments (Selvaraj et al., 2009), which is compatible with the existence of a dense cytoskeletal structure. However, the presence of F-actin in this region has never been clearly demonstrated and visualized in live cells. Here, we showed the existence of an F-actin structure and, in addition, we provided evidence of its dynamic behavior prior to the initiation of the AR. We have observed that the F-actin network in this boundary is depolymerized before the AR begins. We hypothesize that this structure has a function related to the preparation undertaken by the sperm for fusion with the oocyte. In this regard, IZUMO1 is the only sperm protein with a demonstrated role in sperm–egg fusion (Inoue et al., 2005). It was previously observed that IZUMO1 localizes to the anterior acrosome in intact sperm, but once the the AR is initiated, it moves to the equatorial peri-acrosomal segment, the region by which this cell binds and fuses with the egg oolema (Miranda et al., 2009; Sosnik et al., 2009). Sperm from TSSK6-null mice that are deficient in IZUMO1 movement cannot fuse with eggs and display abnormalities in actin polymerization (Sosnik et al., 2009). In addition, IZUMO1 re-localization is blocked in the presence of inhibitors of actin dynamics, such as cytochalasin D, latrunculin A and the myosin kinase blocker blebbistatin (Sosnik et al., 2009), even in sperm that undergo the AR. Our work, together with others (Sosnik et al., 2009; Zhou et al., 2017) suggests that exocytosis completion can be dissociated from IZUMO1

movement. Our hypothesis is that actin depolymerization is essential for facilitating the migration of IZUMO1 to the equatorial domain. Interestingly, the distribution of the sperm-specific plus-end actin-capping protein CAPZA3 shows a dynamic pattern of localization (Sosnik et al., 2010). CAPZA3 is completely relocated to the post-acrosomal region when IZUMO1 has only started to redistribute, suggesting that the redistribution of these two proteins might occur through different mechanisms. In this new location, CAPZA3 could play a role in stabilizing polymerized actin and a subsequent myosin-dependent movement of IZUMO1 to the fusogenic site using the actin cytoskeleton.

The other regions that also displayed an active depolymerization during AR were the lower and upper acrosome regions. We observed that the signal in the acrosomal region that is close to the anterior tip of the head is lost in all cells that undergo AR. Similar to what occurs with the septum, we also observed that this depolymerization occurs prior to the initiation of membrane fusion (∼50 s) in all cells analyzed. In contrast, the F-actin network present in the upper acrosome (for cells that displayed a cortical staining over the entire acrosomal cap that resembles the subcortical F-actin localization) is lost during or after the initiation of the AR, as judged by the increase in FM4-64 fluorescence. Our data suggest that, although this loss in SiR-actin fluorescence may be indicative of depolymerization, it may also occur as a result of membrane loss caused by the AR. Supporting this latter possibility,

super-resolution analysis revealed that the cortical actin remained unaltered during the initial steps of membrane vesiculation, although this observation requires further investigation (Fig. 6 and Movie 5). Interestingly, the proportion of sperm with a pattern containing the septum or the lower acrosome F-actin structure also increased with capacitation (Fig. 2E,F). Those patterns are the ones that are depolymerized with AR induction prior to its initiation.

Finally, in somatic cells, actin depolymerization occurs as a result of the activation of Ca^{2+}-dependent actin-severing proteins, such as gelsolin, cofilin and scinderin, which have been described in human, mouse and guinea pig sperm (Finkelstein et al., 2010; Pelletier et al., 1999; Romarowski et al., 2015). In particular, Ca^{2+}-dependent activation of gelsolin has been proposed to lead to the AR (Finkelstein et al., 2010). Consistent with this, our preliminary data indicate that actin depolymerization follows an initial increase in intracellular Ca^{2+} and precedes fusion between the outer acrosomal membrane and the plasma membrane. We have also reported, in a single-cell analysis, that a specific transitory increase in intracellular Ca^{2+} triggers the AR (Romarowski et al., 2016a). Despite these observations, little is known about the relationship between Ca^{2+}, actin dynamics and the different membranes that conform the sperm apical head.

In summary, we have simultaneously visualized actin dynamics and AR in live sperm by super-resolution microscopy. Based on our observations, we believe that in a specialized cell, like the mammalian sperm, actin depolymerization (septum, lower acrosome) and actin reorganization (perforatorium) in specific regions of the cell coexist. These observations are summarized in the schematic model represented in Fig. 8; when capacitated sperm are exposed to stimuli that promote AR, actin depolymerization occurs in two specific regions of the sperm head, prior to the initiation of the AR, the lower acrosome and the septum. Following the initiation of the AR, the cortical F-actin (upper acrosome) is lost as a result of the formation of hybrid vesicles and not as a result of active depolymerization. This novel approach of using SiR-actin opens new avenues to integrate the two events of the AR and actin dynamics to other molecular processes associated with exocytosis (i.e. changes in Ca^{2+} and membrane potential, etc.) in order to

further understand the process of fertilization. We expect that these novel real-time super-resolution methodologies will be useful in investigating the spatial and temporal relationship between the increase in Ca^{2+} and actin dynamics during the AR. In addition, this approach can also be adapted to other cell types where live imaging of the actin cytoskeleton is required. SiR-actin provides many advantages compared to other methods: (1) it is easy to use, (2) it is membrane permeable, (3) it can be used in live cells without any fixation, and (4) its far-red absorption and emission wavelengths does not overlap with other commonly used fluorophores. On the other hand, the only potential disadvantage to be considered is the possible alteration of actin dynamics, although it is reported that this possibility does not occur or is minimized by using low concentrations of the probe (Melak et al., 2017).

MATERIALS AND METHODS
Reagents
All chemicals were purchased from Sigma-Aldrich Chemical Co. (St Louis, MO) unless stated otherwise. SiR-actin was obtained from Cytoskeleton (Denver, CO). FM4-64, Alexa-Fluor-488–phalloidin and Alexa-Fluor-647–phalloidin were from Thermo Fisher Scientific (Waltham, MA). Ionomycin was from Alomone Laboratories (Jerusalem, Israel).

Animals
CD1 and Lifeact-EGFP (Riedl et al., 2010) mature (10–12 weeks old) male mice were used in this work. Animals were maintained at 23°C with a 12-h-light–12-h-dark cycle. Animal experimental procedures were reviewed and approved by the Ethical Committee of Instituto de Biotecnologia/ UNAM and of the Instituto de Biologia y Medicina Experimental and in strict accordance with the Animal Care and Use Committee (IACUC) guidelines of University of Massachusetts, Amherst and Colorado State University and the Guide for Care and Use of Laboratory Animals approved by the National Institutes of Health (NIH).

Sperm capacitation
In all the experiments, cauda epididymal mouse sperm were collected from retired male breeders by placing minced cauda epididymis in a modified Krebs–Ringer medium (Whitten's-HEPES-buffered medium; WH) as previously described (Romarowski et al., 2015). The capacitating medium
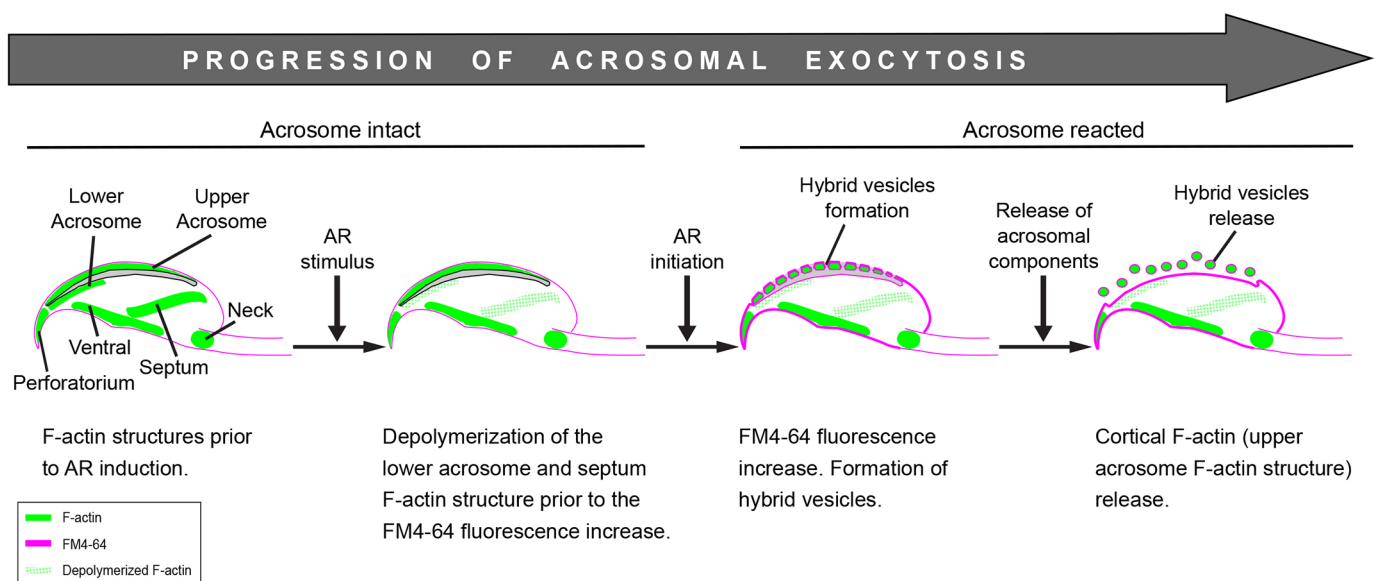

Fig. 8. Schematic diagram of the progression of acrosomal exocytosis. When capacitated sperm are exposed to stimuli that promote AR, actin depolymerization occurs in two specific regions of the sperm head, prior to the initiation of the AR: the lower acrosome and the septum. Following the initiation of the AR, the cortical F-actin (upper acrosome) is lost as a result of the formation hybrid vesicles and not as a result of active depolymerization.

(CAP) was supplemented with 5 mg/ml bovine serum albumin (BSA) and 24 mM $NaHCO_3$, whereas the non-capacitating condition (NC) lacked $NaHCO_3$. The pH was maintained at 7.4 for both cases.

CASA

Aliquots of 3 μl of the sperm suspension were placed into a Leja slide with 20 μm chamber depth pre-warmed to 37°C. The total motility of sperm loaded with 100 nM SiR-actin or vehicle (DMSO) was measured using the Sperm Class Analyzer (SCA) software (MICROPTIC S.L., Barcelona, Spain). The settings used for the analysis were as follows: frames acquired, 30; frame rate, 60 Hz; minimum area, 30 μm^2; maximum area, 170 μm^2; VCL or VAP, VCL; for VCL: statics <10 μm/s, slow-medium 15 μm/s, fast >45 μm/s; progressive >50% of STR; points VAP 5; connectivity 18. At least 300 cells were analyzed.

Evaluation of F-actin levels by monitoring SiR-actin fluorescence using image-based flow cytometry

Sperm were incubated with 100 nM SiR-actin during 10 min in NC medium. Once loaded, sperm were incubated for 60 min in the appropriate medium (CAP or NC). The concentration of SiR-actin in the medium was 100 nM during the whole experiment in order to get a constant signal and to avoid the probe interfering with actin dynamics. To evaluate F-actin levels, the SiR-actin loaded sperm were analyzed on an image-based flow cytometer (Image Stream Mark II, Amnis, Seattle, WA). To determine sperm viability, 100 nM of propidium iodide (PI) was added to the sperm suspension. 488 nm and 642 nm solid-state lasers were used for excitation of PI and SiR-actin, respectively. To reduce auto-fluorescence of unstained cells, the power of the lasers was adjusted to 50 mW (488 nm) and 150 mW (642 nm). The instrument and INSPIRE software were set up as follows: channels 01 and 09 for Brightfield, channel 05 for PI and channel 11 for SiR-actin. A 60× magnification was used. The flow rate was set to low speed/high sensitivity and stream alignment was adjusted when necessary. During acquisition, an area and aspect ratio thresholds ($\geq$50–$\leq$300 μm^2, and $\leq$0.3, respectively) were set to acquire events compatible with sperm morphology. Only single cells, excluding cellular aggregates, or debris were analyzed. Additionally, a focus threshold for the exclusion of out of focus events [gradient root mean square (gradient RMS) for channel 01 of $\geq$60] was held. An additional gating of alive cells was made. Within these parameters, the acquisition rate was of ∼1000–2000 cells per minute (PI-negative cells). A total of 10,000 cells were recorded for each condition. Sperm images were analyzed using the provided analysis software IDEAS and the SiR-actin fluorescence intensity for each sperm was obtained.

Comparison between SiR-actin and Alexa-Fluor-488–phalloidin staining

To compare the staining of SiR-actin with the more widely used phalloidin, a standard phalloidin staining protocol was used as previously described (Romarowski et al., 2015). Cells were fixed in 0.1% glutaraldehyde and 1.5% formaldehyde in PBS for 1 h and collected by centrifugation at 1300 *g* for 5 min. The sperm pellet was immediately re-suspended and incubated with 50 mM NH_4Cl in PBS for 15 min and washed twice by resuspension/centrifugation in PBS and once in distilled water. Water re-suspended cells were used to prepare smears, which were air dried at room temperature overnight. Smears were rinsed with PBS for 7 min then permeabilized using acetone at −20°C for 7 min, and washed three times in PBS. Slides were incubated with 2 units of Alexa-Fluor-488–phalloidin in 100 μl of PBS and 100 nM of SiR-actin, under glass coverslips for 1 h at room temperature in humid conditions in the dark. Smears were washed three times with PBS, once in distilled water and air dried at room temperature. For observation, they were mounted under glass coverslips using Citifluor AF1. Slides were examined using a Yokogawa spinning disk confocal microscope (Zeiss Observer Z.1) and images were captured at 63×/1.4 NA (oil).

Live imaging of F-actin in single mouse sperm

For F-actin visualization in live cells, motile sperm were incubated with 100 nM SiR-actin for 10 min in NC medium and then incubated for 60 min in the appropriate medium, depending on the experiment performed, containing 100 nM SiR-actin. Sperm were immobilized on concanavalin A

(1 mg/ml)-coated coverslips to allow recordings. Unattached spermatozoa were removed by gentle washing, and the chamber was filled with the recording medium (NC medium lacking BSA) containing 100 nM SiR-actin. Recordings were performed at 37°C using a temperature controller (OKO-TOUC, Okolab Inc., USA). Sperm were viewed with a Zeiss Observer Z.1 inverted microscope (Yokogawa spinning disc confocal) and an oil-immersion fluorescence objective (Zeiss plan Apocromat TIRF DIC H/N2 63×/1.4 NA, oil DIC). A pre-centered fiber illuminator (Intelligent Imaging Innovations, Inc.) was used as the light source. For collection excitation and emission SiR-actin fluorescence, a 640 nm laser and a Cy5 filter were used. Fluorescence images were acquired with an Andor Ixon 3 EMCCD camera, model DU-897E-CS0-#BV (Andor Technology) under protocols written in SlideBook software version 6. For these experiments, we recorded one image every 5 s with an exposure time of 100 ms. An image of the plane was taken every 0.27 μm with a total of 20 planes considering an approximate sperm depth of 5 μm in the z plane; 100 fields were acquired simultaneously, using an autofocus defined in a range of 10 μm in the xy plane. The images were obtained offline by generating the maximum z-projection of the image stacks. As a control, we also used sperm from Lifeact-EGFP mice. For these experiments, a Nikon Eclipse Ti-E inverted confocal microscope was used with an iXon Ultra 897 camera.

In vivo super-resolution microscopy of F-actin in single mouse sperm

Sperm live imaging was performed using the sperm loaded with SiR-actin as described above.

Super-resolution imaging measurements were performed on an Olympus IX-81 inverted microscope configured for total internal reflection fluorescence (TIRF) excitation (cellTIRF Illuminator, Olympus). The excitation angle was set up such that the evanescence field had a penetration depth of ∼500 nm (Xcellence software v1.2, Olympus Soft Imaging Solution GMBH). The samples were illuminated stroboscopically using excitation sources depending on the fluorophore used. FM4-64 and SiR-actin were excited with 568 or 640 nm diode-pumped solid-state lasers, respectively. The maximum laser power, measured at the back aperture of the objective lens, ranged between 20 to 25 mW, depending on the laser line used. Beam selection and modulation of laser intensities were controlled via Xcellence software v.1.2. A full multiband laser cube set was used to discriminate the selected light sources (LF 405/488/561/635 A-OMF, Bright Line; Semrock). Fluorescence was collected using an Olympus UApo N 100×/1.49 NA oil-immersion objective lens with an extra 1.6× intermediate magnification lens. Images were acquired with an Andor Ixon 3 EMCCD camera model DU-897ECSO#BV (Andor Technology) under protocols written in Xcellence software version 1.2 (Olympus soft imaging solutions).

3B analysis

Sub-diffraction images were derived from the Bayesian analysis of the stochastic Blinking and Bleaching (termed 3B analysis). Each super-resolution image required 300 images limited by diffraction at an acquisition rate of 1 image every 61 ms, which involved obtaining a super-resolution image every 18.3 s.

Each of the image sequences was fed into the 3B microscopy analysis plugin of ImageJ (Cox et al., 2012), with a pixel size of 100 nm and a full-width half maximum of the point spread function of 290 nm (for FM4-64) and 200 nm (for SiR-actin), both measured experimentally with 0.17 μm fluorescent beads (PS-Speck microscope point source kit; Molecular Probes, Inc.). All other parameters were set up as the default values. The 3B analysis was run in parallel over 200 iterations as recommended, and the final super-resolution reconstructions were created at a pixel size of 10 nm. The spatial resolution observed in our imaging setup by 3B analysis was ∼50 nm.

SRRF

For each super-resolution reconstruction, five serial stacks were acquired within an evanescent field of 500 nm, with an axial z spacing of 100 nm. Each serial stack, composed of 300 temporal images collected with an exposure time of 5 to 20 ms at 10 Hz, was reconstructed with NanoJ-SRRF

plugins of ImageJ (Gustafsson et al., 2016). For the analysis, we used the following parameters: Annular radius: 0.5, Radiality magnification: 10×, Annular axis: 8. For the temporal analysis, we used the Temporal Radiality Auto-Correlations algorithm of 2nd order, with temporal integrated correlation and intensity ponderation. All other parameters were set up as the default options. The radiality maps were drift corrected using pre-calculated drift tables obtained with the Estimate Drift tool of NanoJ-SRRF, considering a time averaging of 300 images.

STORM

Because SiR-actin is not suitable for STORM, phalloidin was used as described below. Sperm samples were seeded in poly-lysinated coverslips (Corning #1.5) and air dried for 5 min. Then, samples were fixed and permeabilized with 0.3% (v/v) glutaraldehyde and 0.25% (v/v) Triton X-100 in cytoskeleton buffer [CB; MES (10 mM, pH6.1), NaCl (150 mM), EGTA (5 mM), glucose (5 mM), and $MgCl_2$ (5 mM)] for 1 min. Cells were washed with CB three times for 5 min each, and then incubated with 2% (v/v) glutaraldehyde in CB for 15 min. Then cells were then washed with CB twice for 10 min each. To avoid background fluorescence caused by glutaraldehyde fixation, samples were incubated with 0.1% (w/v) of sodium borohydride in PBS for 7 min. After that, samples were washed with PBS twice for 5 min each, and incubated with 0.5 µM Alexa-Fluor-647–phalloidin in PBS for 1 h. Cells were then washed with PBS three times for 5 min each and immediately mounted in STORM imaging buffer. Images were acquired using Andor IQ 2.3 software in a custom-built microscope equipped with an Olympus PlanApo 100×/1.45 NA objective and a CRISP ASI autofocus system (Weigel et al., 2011). Alexa Fluor 647 was excited with a 640 nm laser (DL640-150-O, CrystaLaser, Reno, NV) under continuous illumination. Initially, the photo-switching rate was sufficient to provide a substantial fluorophore density. However, as fluorophores irreversibly photo-bleached, a 405 nm laser was introduced to enhance photo-switching. The intensity of the 405 nm laser was adjusted in the range of 0.01–0.5 mW to maintain an appropriate density of active fluorophores. A cylindrical lens with a focal lens of 1 m was placed in the detection path in order to achieve a 3D resolution (Huang et al., 2008). A calibration curve for axial localization was generated with 50 nm gold nanoparticles (Nanopartz, Loveland, CO) immobilized on a coverslip. The images were acquired by a water-cooled, back-illuminated EMCCD camera (Andor iXon DU-888) operated at −85°C at a rate of 23 frames/s; 50,000 frames were collected to generate a super-resolution image. Super-resolution image reconstruction, single-molecule localization, and drift correction using image cross correlation and reconstruction were all performed with ThunderSTORM plugin in ImageJ (Ovesný et al., 2014).

TIRF microscopy to visualize cortical F-actin and plasma membrane in single mouse sperm

Recordings were performed using the sperm loaded with SiR-actin as described above, but in this case the recording medium contained 1 µM FM4-64. For these experiments, the inverted Olympus IX81 TIRF microscope equipped with an Andor IXON 3 camera was used, as explained in previous sections. Fluorescence was collected using an Olympus UApo N 100×/1.49 NA oil-immersion objective lens with an extra 1.6× intermediate magnification lens. For SiR-actin excitation, a 640 nm laser was used and, for FM4-64 excitation, a 491 nm laser was used. The emission filter window of 670–700 nm was used. The delay between one channel and the other was of 30 ms. The diffraction-limited images obtained by TIRF microscopy were used for super-resolution reconstruction as explained above.

Live imaging of F-actin dynamics and acrosomal exocytosis in single mouse sperm

Recordings were performed using capacitated sperm loaded with SiR-actin as described above, but in this case the recording medium contained 1 µM FM4-64. Sperm were recorded over time, before and after the addition of 10 µM ionomycin or 100 µM progesterone. SiR-actin and FM4-64 fluorescence acquisitions were performed as described above. Two images per second were acquired for periods of 20 min, using the inverted Olympus

IX81 TIRF microscope. An oil immersion fluorescence objective (60×/1.45 NA) was used. During all the experiments, 16-bit images were obtained and movies were processed and analyzed with macros written in ImageJ (National Institutes of Health). Regions of interest were drawn on each sperm in the movie for quantification. A plot of the fluorescence intensity of each spermatozoon versus time was generated in Origin 6.0 (OriginLab Corporation). Fluorescence is expressed as $(F-F_0)/F_0$, where F_0 is the average fluorescence intensity value of the frames before the addition of ionomycin. When brightness and contrast were adjusted, this was done equally in all images or movies filmed under the same conditions.

Statistical analysis

Data are expressed as mean±s.e.m. or ±s.d. for at least three experiments for all determinations. Statistical analyses were performed with GraphPad Prism version 4.0 for Windows, GraphPad Software (San Diego, CA) or by using the R language environment [R 3.3.3 GUI 1.69 Mavericks build (7328)]. The statistical analysis performed is indicated in the corresponding figure legend. $P<0.05$ was considered statistically significant.

Author contributions

Conceptualization: P.E.V., Dario Krapf, A.G., A.D., M.G.B.; Methodology: P.T.R., M.G.G., X.X., G.C.-J., C.S.-C., A.G.; Software: Diego Krapf, A.G.; Validation: G.M.L., H.V.R.-G., A.G.; Formal analysis: A.R., Diego Krapf; Investigation: A.R., A.G.V.F., P.T.R., M.G.G., G.M.L., H.V.R.-G.; Resources: C.S.-C., P.E.V., A.G., A.D.; Data curation: A.G.V.F.; Writing - original draft: A.R., A.D., M.G.B.; Writing - review & editing: Diego Krapf, P.E.V., Dario Krapf, A.G., A.D., M.G.B.; Visualization: X.X., C.S.-C., Diego Krapf, Dario Krapf; Supervision: A.D., M.G.B.; Project administration: M.G.B.; Funding acquisition: M.G.B.

Supplementary information

Supplementary information available online at
http://jcs.biologists.org/lookup/doi/10.1242/jcs.218958.supplemental

References

Baltiérrez-Hoyos, R., Roa-Espitia, A. L. and Hernández-González, E. O. (2012). The association between CDC42 and caveolin-1 is involved in the regulation of capacitation and acrosome reaction of guinea pig and mouse sperm. *Reproduction* **144**, 123-134.

Belmonte, S. A., Mayorga, L. S. and Tomes, C. N. (2016). The molecules of sperm exocytosis. *Adv. Anat. Embryol. Cell Biol.* **220**, 71-92.

Branham, M. T., Mayorga, L. S. and Tomes, C. N. (2006). Calcium-induced acrosomal exocytosis requires cAMP acting through a protein kinase A-independent, Epac-mediated pathway. *J. Biol. Chem.* **281**, 8656-8666.

Branham, M. T., Bustos, M. A., De Blas, G. A., Rehmann, H., Zarelli, V. E. P., Treviño, C. L., Darszon, A., Mayorga, L. S. and Tomes, C. N. (2009). Epac

activates the small G proteins Rap1 and Rab3A to achieve exocytosis. *J. Biol. Chem.* **284**, 24825-24839.

Brener, E., Rubinstein, S., Cohen, G., Shternall, K., Rivlin, J. and Breitbart, H. (2003). Remodeling of the actin cytoskeleton during mammalian sperm capacitation and acrosome reaction. *Biol. Reprod.* **68**, 837-845.

Buffone, M. G., Hirohashi, N. and Gerton, G. L. (2014). Unresolved questions concerning mammalian sperm acrosomal exocytosis. *Biol. Reprod.* **90**, 112.

Chowdhury, H. H., Popoff, M. R. and Zorec, R. (1999). Actin cytoskeleton depolymerization with clostridium spiroforme toxin enhances the secretory activity of rat melanotrophs. *J. Physiol.* **521**, 389-395.

Chung, J.-J., Shim, S.-H., Everley, R. A., Gygi, S. P., Zhuang, X. and Clapham, D. E. (2014). Structurally distinct Ca2+ signaling domains of sperm flagella orchestrate tyrosine phosphorylation and motility. *Cell* **157**, 808-822.

Chung, J.-J., Miki, K., Kim, D., Shim, S.-H., Shi, H. F., Hwang, J. Y., Cai, X., Iseri, Y., Zhuang, X. and Clapham, D. E. (2017). CatSperζ regulates the structural continuity of sperm Ca2+ signaling domains and is required for normal fertility. *eLife* **6**, e23082.

Clermont, Y., Oko, R. and Hermo, L. (1990). Immunocytochemical localization of proteins utilized in the formation of outer dense fibers and fibrous sheath in rat spermatids: an electron microscope study. *Anat. Rec.* **227**, 447-457.

Cohen, G., Rubinstein, S., Gur, Y. and Breitbart, H. (2004). Crosstalk between protein kinase A and C regulates phospholipase D and F-actin formation during sperm capacitation. *Dev. Biol.* **267**, 230-241.

Cooper, J. A. (1987). Effects of cytochalasin and phalloidin on actin. *J. Cell Biol.* **105**, 1473-1478.

Cox, S., Rosten, E., Monypenny, J., Jovanovic-Talisman, T., Burnette, D. T., Lippincott-Schwartz, J., Jones, G. E. and Heintzmann, R. (2012). Bayesian localization microscopy reveals nanoscale podosome dynamics. *Nat. Methods* **9**, 195-200.

Dan, J. C. (1952). Studies on the acrosome. I. Reaction to egg-water. *Biol. Bull.* **103**, 54-66.

De Blas, G. A., Roggero, C. M., Tomes, C. N. and Mayorga, L. S. (2005). Dynamics of SNARE assembly and disassembly during sperm acrosomal exocytosis. *PLoS Biol.* **3**, e323.

De Jonge, C. J., Han, H.-L., Lawrie, H., Mack, S. R. and Zaneveld, L. J. D. (1991). Modulation of the human sperm acrosome reaction by effectors of the adenylate cyclase/cyclic AMP second-messenger pathway. *J. Exp. Zool.* **258**, 113-125.

De La Vega-Beltran, J. L., Sánchez-Cárdenas, C., Krapf, D., Hernandez-González, E. O., Wertheimer, E., Treviño, C. L., Visconti, P. E. and Darszon, A. (2012). Mouse sperm membrane potential hyperpolarization is necessary and sufficient to prepare sperm for the acrosome reaction. *J. Biol. Chem.* **287**, 44384-44393.

D'Este, E., Kamin, D., Göttfert, F., El-Hady, A. and Hell, S. W. (2015). STED nanoscopy reveals the ubiquity of subcortical cytoskeleton periodicity in living neurons. *Cell Rep.* **10**, 1246-1251.

Ehre, C., Rossi, A. H., Abdullah, L. H., De Pestel, K., Hill, S., Olsen, J. C. and Davis, C. W. (2004). Barrier role of actin filaments in regulated mucin secretion from airway goblet cells. *Am. J. Physiol. Cell Physiol.* **288**, C46-C56.

Fiedler, S. E., Bajpai, M. and Carr, D. W. (2008). Identification and characterization of RHOA-interacting proteins in bovine spermatozoa. *Biol. Reprod.* **78**, 184-192.

Finkelstein, M., Etkovitz, N. and Breitbart, H. (2010). Role and regulation of sperm gelsolin prior to fertilization. *J. Biol. Chem.* **285**, 39702-39709.

Fukami, K., Nakao, K., Inoue, T., Kataoka, Y., Kurokawa, M., Fissore, R. A., Nakamura, K., Katsuki, M., Mikoshiba, K., Yoshida, N. et al. (2001). Requirement of phospholipase Cdelta4 for the zona pellucida-induced acrosome reaction. *Science* **292**, 920-923.

Fukami, K., Yoshida, M., Inoue, T., Kurokawa, M., Fissore, R. A., Yoshida, N., Mikoshiba, K. and Takenawa, T. (2003). Phospholipase Cδ4 is required for Ca 2+ mobilization essential for acrosome reaction in sperm. *J. Cell Biol.* **161**, 79-88.

Gasman, S., Chasserot-Golaz, S., Malacombe, M., Way, M. and Bader, M.-F. (2004). Regulated exocytosis in neuroendocrine cells: a role for subplasmalemmal Cdc42/N-WASP–induced actin filaments. *Mol. Biol. Cell* **15**, 520-531.

Gervasi, M. G., Xu, X., Carbajal-Gonzalez, B., Buffone, M. G., Visconti, P. E. and Krapf, D. (2018). The actin cytoskeleton of the mouse sperm flagellum is organized in a helical structure. *J. Cell Sci.* **131**, jcs.215897.

Gustafsson, N., Culley, S., Ashdown, G., Owen, D. M., Pereira, P. M. and Henriques, R. (2016). Fast live-cell conventional fluorophore nanoscopy with ImageJ through super-resolution radial fluctuations. *Nat. Commun.* **7**, 12471.

Hino, T., Muro, Y., Tamura-Nakano, M., Okabe, M., Tateno, H. and Yanagimachi, R. (2016). The behavior and acrosomal status of mouse spermatozoa in vitro, and within the oviduct during fertilization after natural mating. *Biol. Reprod.* **95**, 50-50.

Hirohashi, N., La Spina, F. A., Romarowski, A. and Buffone, M. G. (2015). Redistribution of the intra-acrosomal EGFP before acrosomal exocytosis in mouse spermatozoa. *Reproduction* **149**, 657-663.

Huang, B., Wang, W., Bates, M. and Zhuang, X. (2008). Three-dimensional super-resolution imaging by stochastic optical reconstruction microscopy. *Science* **319**, 810-813.

Inoue, N., Ikawa, M., Isotani, A. and Okabe, M. (2005). The immunoglobulin superfamily protein Izumo is required for sperm to fuse with eggs. *Nature* **434**, 234-238.

Jones, R., James, P. S., Howes, L., Bruckbauer, A. and Klenerman, D. (2007). Supramolecular organization of the sperm plasma membrane during maturation and capacitation. *Asian J. Androl.* **9**, 438-444.

Korley, R., Pouresmaeili, F. and Oko, R. (1997). Analysis of the protein composition of the mouse sperm perinuclear theca and characterization of its major protein constituent. *Biol. Reprod.* **57**, 1426-1432.

La Spina, F. A., Puga Molina, L. C., Romarowski, A., Vitale, A. M., Falzone, T. L., Krapf, D., Hirohashi, N. and Buffone, M. G. (2016). Mouse sperm begin to undergo acrosomal exocytosis in the upper isthmus of the oviduct. *Dev. Biol.* **411**, 172-182.

Lucchesi, O., Ruete, M. C., Bustos, M. A., Quevedo, M. F. and Tomes, C. N. (2016). The signaling module cAMP/Epac/Rap1/PLCε/IP3 mobilizes acrosomal calcium during sperm exocytosis. *Biochim. Biophys. Acta Mol. Cell Res.* **1863**, 544-561.

Lukinavičius, G., Reymond, L., D'Este, E., Masharina, A., Göttfert, F., Ta, H., Güther, A., Fournier, M., Rizzo, S., Waldmann, H. et al. (2014). Fluorogenic probes for live-cell imaging of the cytoskeleton. *Nat. Methods* **11**, 731-733.

Magliocca, V., Petrini, S., Franchin, T., Borghi, R., Niceforo, A., Abbaszadeh, Z., Bertini, E. and Compagnucci, C. (2017). Identifying the dynamics of actin and tubulin polymerization in iPSCs and in iPSC-derived neurons. *Oncotarget* **8**, 111096-111109.

Mata-Martínez, E., Darszon, A. and Treviño, C. L. (2018). pH-dependent Ca +2 oscillations prevent untimely acrosome reaction in human sperm. *Biochem. Biophys. Res. Commun.* **497**, 146-152.

Melak, M., Plessner, M. and Grosse, R. (2017). Actin visualization at a glance. *J. Cell Sci.* **130**, 525-530.

Miranda, P. V., Allaire, A., Sosnik, J. and Visconti, P. E. (2009). Localization of low-density detergent-resistant membrane proteins in intact and acrosome-reacted mouse sperm. *Biol. Reprod.* **80**, 897-904.

Muallem, S., Kwiatkowska, K., Xu, X. and Yin, H. L. (1995). Actin filament disassembly is a sufficient final trigger for exocytosis in nonexcitable cells. *J. Cell Biol.* **128**, 589-598.

Muro, Y., Hasuwa, H., Isotani, A., Miyata, H., Yamagata, K., Ikawa, M., Yanagimachi, R. and Okabe, M. (2016). Behavior of mouse spermatozoa in the female reproductive tract from soon after mating to the beginning of fertilization. *Biol. Reprod.* **94**, 80.

Oko, R. and Morales, C. R. (1994). A novel testicular protein, with sequence similarities to a family of lipid binding proteins, is a major component of the rat sperm perinuclear Theca. *Dev. Biol.* **166**, 235-245.

Ovesný, M., Křížek, P., Borkovec, J., Švindrych, Z. and Hagen, G. M. (2014). ThunderSTORM: a comprehensive ImageJ plug-in for PALM and STORM data analysis and super-resolution imaging. *Bioinformatics* **30**, 2389-2390.

Pelletán, L. E., Suhaiman, L., Vaquer, C. C., Bustos, M. A., De Blas, G. A., Vitale, N., Mayorga, L. S. and Belmonte, S. A. (2015). ADP ribosylation factor 6 (ARF6) promotes acrosomal exocytosis by modulating lipid turnover and Rab3A activation. *J. Biol. Chem.* **290**, 9823-9841.

Pelletier, R.-M., Trifaro, J.-M., Carbajal, M. E., Okawara, Y. and Vitale, M. L. (1999). Calcium-dependent actin filament-severing protein scinderin levels and localization in bovine testis, epididymis, and spermatozoa. *Biol. Reprod.* **60**, 1128-1136.

Puga Molina, L. C., Luque, G. M., Balestrini, P. A., Marín-Briggiler, C. I., Romarowski, A. and Buffone, M. G. (2018). Molecular basis of human sperm capacitation. *Front. Cell Dev. Biol.* **6**, 72.

Quevedo, M. F., Lucchesi, O., Bustos, M. A., Pocognoni, C. A., De la Iglesia, P. X. and Tomes, C. N. (2016). The Rab3A-22A chimera prevents sperm exocytosis by stabilizing open fusion pores. *J. Biol. Chem.* **291**, 23101-23111.

Riedl, J., Flynn, K. C., Raducanu, A., Gärtner, F., Beck, G., Bösl, M., Bradke, F., Massberg, S., Aszodi, A., Sixt, M. et al. (2010). Lifeact mice for studying F-actin dynamics. *Nat. Methods* **7**, 168-169.

Romarowski, A., Battistone, M. A., La Spina, F. A., Puga Molina, L. D. C., Luque, G. M., Vitale, A. M., Cuasnicu, P. S., Visconti, P. E., Krapf, D. and Buffone, M. G. (2015). PKA-dependent phosphorylation of LIMK1 and Cofilin is essential for mouse sperm acrosomal exocytosis. *Dev. Biol.* **405**, 237-249.

Romarowski, A., Sánchez-Cárdenas, C., Ramírez-Gómez, H. V., Puga Molina, L. D. C., Treviño, C. L., Hernández-Cruz, A., Darszon, A. I. and Buffone, M. G. (2016a). A specific transitory increase in intracellular calcium induced by progesterone promotes acrosomal exocytosis in mouse sperm. *Biol. Reprod.* **94**, 1-12.

Romarowski, A., Luque, G. M., La Spina, F. A., Krapf, D. and Buffone, M. G. (2016b). Role of actin cytoskeleton during mammalian sperm acrosomal exocytosis. *Adv. Anat. Embryol. Cell Biol.* **220**, 129-144.

Sánchez-Cárdenas, C., Servín-Vences, M. R., José, O., Treviño, C. L., Hernández-Cruz, A. and Darszon, A. (2014). Acrosome reaction and Ca2+ imaging in single human spermatozoa: new regulatory roles of [Ca2+]i. *Biol. Reprod.* **91**, 67.

Satouh, Y., Inoue, N., Ikawa, M. and Okabe, M. (2012). Visualization of the moment of mouse sperm-egg fusion and dynamic localization of IZUMO1. *J. Cell Sci.* **125**, 4985-4990.

Selvaraj, V., Asano, A., Buttke, D. E., Sengupta, P., Weiss, R. S. and Travis, A. J. (2009). Mechanisms underlying the micron-scale segregation of sterols and G $_{M1}$ in live mammalian sperm. *J. Cell. Physiol.* **218**, 522-536.

Sosnik, J., Miranda, P. V., Spiridonov, N. A., Yoon, S.-Y., Fissore, R. A., Johnson, G. R. and Visconti, P. E. (2009). Tssk6 is required for Izumo relocalization and gamete fusion in the mouse. *J. Cell Sci.* **122**, 2741-2749.

Sosnik, J., Buffone, M. G. and Visconti, P. E. (2010). Analysis of CAPZA3 localization reveals temporally discrete events during the acrosome reaction. *J. Cell. Physiol.* **224**, 575-580.

Spungin, B., Margalit, I. and Breitbart, H. (1995). Sperm exocytosis reconstructed in a cell-free system: evidence for the involvement of phospholipase C and actin filaments in membrane fusion. *J. Cell Sci.* **108**, 2525-2535.

Stival, C., La Spina, F. A., Baró Graf, C., Arcelay, E., Arranz, S. E., Ferreira, J. J., Le Grand, S., Dzikunu, V. A., Santi, C. M., Visconti, P. E. et al. (2015). Src kinase is the connecting player between Protein Kinase A (PKA) activation and hyperpolarization through SLO3 potassium channel regulation in mouse sperm. *J. Biol. Chem.* **290**, 18855-18864.

Suzuki, K. G. N., Ando, H., Komura, N., Fujiwara, T. K., Kiso, M. and Kusumi, A. (2017). Development of new ganglioside probes and unraveling of raft domain structure by single-molecule imaging. *Biochim. Biophys. Acta* **1861**, 2494-2506.

Torregrosa-Hetland, C. J., Villanueva, J., Giner, D., Lopez-Font, I., Nadal, A., Quesada, I., Viniegra, S., Exposito-Romero, G., Gil, A., Gonzalez-Velez, V. et al. (2011). The F-actin cortical network is a major factor influencing the organization of the secretory machinery in chromaffin cells. *J. Cell Sci.* **124**, 727-734.

Vandekerckhove, J., Deboben, A., Nassal, M. and Wieland, T. (1985). The phalloidin binding site of F-actin. *EMBO J.* **4**, 2815-2818.

Visegrády, B., Lőrinczy, D., Hild, G., Somogyi, B. and Nyitrai, M. (2004). The effect of phalloidin and jasplakinolide on the flexibility and thermal stability of actin filaments. *FEBS Lett.* **565**, 163-166.

Weigel, A. V., Simon, B., Tamkun, M. M. and Krapf, D. (2011). Ergodic and nonergodic processes coexist in the plasma membrane as observed by single-molecule tracking. *Proc. Natl. Acad. Sci. USA* **108**, 6438-6443.

Yamazaki, S., Harata, M., Idehara, T., Konagaya, K., Yokoyama, G., Hoshina, H. and Ogawa, Y. (2018). Actin polymerization is activated by terahertz irradiation. *Sci. Rep.* **8**, 9990.

Zhou, C., Huang, L., Shi, D.-S. and Jiang, J.-R. (2017). Effects of latrunculin A on the relocation of sperm IZUMO1 during gamete interaction in mouse. *Mol. Reprod. Dev.* **84**, 1183-1190.